Photoemission tomography of excitons: Momentum-space signatures of correlated electron-hole wave functions

Siegfried Kaidisch,[1] Amir Kleiner,[1,2] Sivan Refaely-Abramson,[2] Peter Puschnig,[1] and Christian S. Kern[1,*]
[1]*Institute of Physics, NAWI Graz, University of Graz, 8010 Graz, Austria*
[2]*Department of Molecular Chemistry and Materials Science, Weizmann Institute of Science, Rehovot 7610001, Israel*

(Received 22 December 2025; accepted 3 September 2026; published 9 November 2026)

The momentum-space signatures of excitons can be experimentally accessed through time-resolved (pump-probe) photoelectron spectroscopy. In this work, we develop a computational framework for exciton photoemission orbital tomography (exPOT) in periodic systems, enabling the simulation and interpretation of experimental observables within many-body perturbation theory. By connecting the $GW+$ Bethe-Salpeter equation (BSE) approach to photoemission tomography, our formalism captures exciton photoemission in periodic systems, explicitly incorporating photoemission matrix element effects induced by the light-matter interaction via the probe pulse. The correlated nature of electrons and holes introduces distinct consequences for excitonic photoemission. Using the prototypical two-dimensional material hexagonal boron nitride, we demonstrate these effects, including a dependence of the photoemission angular distribution on the pump pulse polarization. Moreover, our framework extends to excitons with finite center-of-mass momentum, making it well-suited to studying momentum-dark excitons. This provides valuable insights into the microscopic nature of excitonic phenomena in quantum materials.

DOI: 10.1103/z2w9-2q3c

I. INTRODUCTION

Excitons—bound electron-hole pairs—play a fundamental role in determining the optical and electronic response of semiconducting and insulating materials. From a theoretical perspective, describing excitonic effects requires going beyond single-particle approximations and typically involves time-dependent density functional theory (TDDFT) with suitable long-range xc-kernels, or many-body perturbation theory (MBPT) within the *GW* plus Bethe-Salpeter equation (BSE) framework [1–3]. Excitation energies and optical spectra computed in such a way can then be compared to absorption or luminescence spectroscopy. While theory naturally provides detailed information about the quantum mechanical nature of the underlying exciton wave function in real and momentum space, optical experiments provide only limited microscopic insights.

Here, time- and angle-resolved photoemission spectroscopy (trARPES) has emerged as a promising tool to dynamically probe excited states in energy and momentum space, thus offering enhanced insight into the microscopic nature of excitons [4–10]. It is therefore highly desirable to have a theory that can connect trARPES signatures with first-principles calculations. The arguably most direct way of simulating trARPES is a numerical photodetection scheme, as implemented in real-time TDDFT [11,12], which not only allows for pump-probe simulations in linear and nonlinear regimes but also captures final-state effects in the photoemission process [13,14]. Unfortunately, the only practically applicable approximation for the xc-kernel in such real-time TDDFT simulations is the adiabatic local density approximation, which fails to capture excitonic effects.

This stands in contrast to Green's function methods, where the inclusion of Coulomb correlation between electron and hole, in conjunction with the screened exchange interaction, successfully describes bound electron-hole states. The nonequilibrium Green's function (NEGF) method is particularly powerful for simulating excited systems through explicit time propagation, capturing the effects of many-body interactions, such as electron-electron and electron-phonon scattering, via self-energy corrections [15]. The photoemission signal is then derived from the lesser Green's function and the matrix element [16], with the former resulting from the nonequilibrium occupation due to the pump pulse and the latter accounting for the effects of the probe pulse. However, due to the complexity of the method, trARPES simulations within the NEGF framework have so far been restricted to model systems or Wannier-Hamiltonians [17,18], often neglecting the transition probability to the photoelectron state induced by the probe pulse [19,20].

In one-step models for photoemission, these effects are encoded in the photoemission matrix element. Matrix element effects are not only crucial for accurately describing the photoemission process itself, but also encode rich information about quantum geometrical effects [21,22], such as the Berry curvature [23,24] or orbital angular momentum

*Contact author: christian.kern@uni-graz.at

Published by the American Physical Society under the terms of the Creative Commons Attribution 4.0 International license. Further distribution of this work must maintain attribution to the author(s) and the published article's title, journal citation, and DOI.

[25,26]. Moreover, in organic or hybrid organic/inorganic systems, matrix element effects may easily become the dominant contribution to the observed angular dependence in the photoemission signal, forming the basis of the successful photoemission orbital tomography (POT) approach [27–29].

For organic molecules, POT has recently been conceptually extended to exciton photoemission orbital tomography (exPOT) [30], which establishes a direct connection between the angular distributions observed in trARPES and the real-space and momentum-space structure of excitonic wave functions. However, this earlier work was limited to nonperiodic systems, such as isolated molecules, thereby excluding its applicability to condensed-phase materials and low-dimensional crystals.

In the present work, we introduce exPOT for periodic systems, an *ab initio* scheme to simulate trARPES from first principles. In contrast to explicit time-propagation methods, we build our framework on exciton wave functions from GW + BSE calculations in frequency space. Among the many possible experimental conditions realized in trARPES experiments [10,31], we thus restrict our approach to pump fields in the linear response regime, excluding Floquet and other nonlinear effects. Moreover, we assume an incoherent exciton population established after fast enough dephasing, such that any coherence with the pump field, and thus any memory of the excitation process, is lost. Finally, the probe photon energies are assumed to lie in the 15 to 50 eV range of typical laser experiments. Under these conditions, we show that the photoemission signal from a pure exciton state (i.e., an eigenstate of the BSE Hamiltonian) can be expressed in terms of the Fourier-transformed single-particle Bloch functions, weighted by the exciton's BSE eigenvector, thus reflecting the entangled many-body character of electron-hole correlation. Given a pump-probe delay time that is longer than the dephasing time but shorter than the excited state's lifetime, the experimentally measured photoemission signal can then be deconvoluted into an incoherent sum over photoemission from contributing pure exciton states. Our numerical implementation builds upon solutions of the BSE expressed in a plane-wave basis set and is therefore suited to treat surfaces of crystalline solids and 2D semiconductors in the repeated-slab approach. We use the plane-wave approximation for the final state in the photoemission process, including effects of the light polarization. We emphasize that our generalized theory can also describe excitons with finite center-of-mass momentum, allowing for the treatment of optically dark excitons—a key feature in transition metal dichalcogenides and other layered materials [8,32–34]. The exPOT approach in periodic systems thus enables access to a new class of excitonic observables in photoemission [35], bridging the gap between theoretical many-body wave functions and experimental momentum-resolved spectra.

This work is structured as follows. First, we formulate the theoretical foundations in Sec. II, starting from Fermi's golden rule for the photoemission process, and including the many-body excitonic effects in terms of a Dyson orbital-like construction for Bloch functions. For energy-degenerate excitons, the resulting expression for photoemission from excitons also carries an additional dependence on the pump polarization, which is discussed thereafter. As an example, we present results in Sec. III, where we apply our method to monolayer hexagonal boron nitride (hBN), a prototypical 2D semiconductor with well-characterized excitonic properties. We further show that the resulting photoelectron angular distribution maps depend not only on the character of the exciton but also on the polarization of the pump pulse, and discuss the implications of our theory on the rich information contained in exciton photoemission.

II. THEORY

A. Derivation of exPOT for periodic systems

In this section, we derive the formalism on which we base our interpretation of photoelectron spectroscopy in terms of exciton wave functions and under the following conditions. First, we assume that the optical excitation (i.e., the pump pulse) is weak, such that we stay in the linear regime and well below the exciton Mott transition threshold. Moreover, the pump pulse is considered to be long enough to minimize energy broadening. Second, we focus on timescales beyond the dephasing of the optical population, where the system has evolved into an incoherent exciton population [36,37], which serves as the initial state for our theoretical treatment.

We consider systems with a finite band gap and model the system's excited state using a correlated electron-hole wave function, expressed in terms of single-particle Bloch states as the basis set. To distinguish between electron and hole states, we write the valence state wave functions as $\phi_{v,\boldsymbol{q}}(\boldsymbol{r})$, with v denoting the band index and $\boldsymbol{q}$ the crystal momentum. Similarly, conduction state wave functions are written as $\xi_{c,\boldsymbol{q}}(\boldsymbol{r})$. With these single-particle basis sets and employing the Tamm-Dancoff approximation (TDA), we can write the m-th exciton wave function $\Psi^{(m,\boldsymbol{Q})}(\boldsymbol{r}_h,\boldsymbol{r}_e)$ in terms of electron- and hole coordinates, $\boldsymbol{r}_e$ and $\boldsymbol{r}_h$, respectively [2]:

$$\Psi^{(m,\boldsymbol{Q})}(\boldsymbol{r}_h,\boldsymbol{r}_e)=\sum_{\boldsymbol{q}}^{\mathrm{BZ}}\sum_{v}^{N_{\mathrm{occ.}}}\sum_{c}^{\infty}X_{v,c,\boldsymbol{q}}^{(m,\boldsymbol{Q})}\phi_{v,\boldsymbol{q}}^{*}(\boldsymbol{r}_h)\xi_{c,\boldsymbol{q}+\boldsymbol{Q}}(\boldsymbol{r}_e),\quad(1)$$

with the normalization $\sum_{\boldsymbol{q}}^{\mathrm{BZ}}\sum_{v}^{N_{\mathrm{occ.}}}\sum_{c}^{\infty}|X_{v,c,\boldsymbol{q}}^{(m,\boldsymbol{Q})}|^2=1$. In this expression, $\boldsymbol{Q}$ represents the center-of-mass momentum of the exciton, and $X_{v,c,\boldsymbol{q}}^{(m,\boldsymbol{Q})}$ encode the exciton character. They are the elements of the transition density matrix, which we obtain as eigenstates from the BSE Hamiltonian, with the corresponding excitation energies denoted as $\Omega^{(m,\boldsymbol{Q})}$. In the language of second quantization, the excitonic state may also be written as

$$\left|\Psi_{m,\boldsymbol{Q}}^{N}\right\rangle=\sum_{\boldsymbol{q}}^{\mathrm{BZ}}\sum_{v,c}X_{v,c,\boldsymbol{q}}^{(m,\boldsymbol{Q})}\hat{a}_{c,\boldsymbol{q}+\boldsymbol{Q}}^{\dagger}\hat{a}_{v,\boldsymbol{q}}\left|\Psi_{0}^{N}\right\rangle.\quad(2)$$

Here, $\hat{a}_{v,\boldsymbol{q}}$ annihilates an electron with crystal momentum $\boldsymbol{q}$ in the valence band v (or creates a hole) in the ground state $|\Psi_0^N\rangle$, and $\hat{a}_{c,\boldsymbol{q}+\boldsymbol{Q}}^{\dagger}$ creates an electron in the conduction band c with momentum $\boldsymbol{q}+\boldsymbol{Q}$.

Analogous to the ground state POT [29], and under the conditions stated above, we treat the photoemission due to the probe pulse in first-order perturbation theory. As outlined in Ref. [38], we apply Fermi's golden rule for the transition rate

from an N-electron initial state $|\Psi_{\mathrm{i}}^N\rangle$ to a final state $|\Psi_{\mathrm{f}}^N\rangle$:

$$W_{\mathrm{i}\to\mathrm{f}} = 2\pi \left|\left\langle \Psi_{\mathrm{f}}^N \middle| \boldsymbol{A}\cdot\hat{\boldsymbol{P}} \middle| \Psi_{\mathrm{i}}^N \right\rangle\right|^2 \delta(\omega + E_{\mathrm{i}} - E_{\mathrm{f}}), \tag{3}$$

with the Dirac delta function enforcing energy conservation between the initial and final states, and the energy ω carried by the photon field $\boldsymbol{A}$. Here, and in the following, we use the velocity gauge within the dipole approximation, with $\hat{\boldsymbol{P}} = \sum_{i=1}^{N} \hat{\boldsymbol{p}}_i$ denoting the N-electron momentum operator, and we use atomic units unless denoted otherwise.

The final state $|\Psi_{\mathrm{f}}^N\rangle$ describes the system after the photoemission event. Here, we make use of the sudden approximation [39] and thus neglect correlations between the photoelectron described by the one-electron state $|\gamma_{\boldsymbol{k}}\rangle$ and the remaining $(N-1)$-electron state $|\Psi_{\mathrm{f}}^{N-1}\rangle$. Therefore, $|\Psi_{\mathrm{f}}^N\rangle$ can be written as an antisymmetrized product:

$$\left|\Psi_{\mathrm{f}}^N\right\rangle = \hat{\mathcal{A}}\left(\left|\Psi_{\mathrm{f}}^{N-1}\right\rangle \otimes |\gamma_{\boldsymbol{k}}\rangle\right) \equiv \left|\mathcal{A}\Psi_{\mathrm{f}}^{N-1}\gamma_{\boldsymbol{k}}\right\rangle, \tag{4}$$

where we additionally assume the $(N-1)$-electron final state to be of the form

$$\left|\Psi_{j,\tilde{\boldsymbol{q}}}^{N-1}\right\rangle \equiv \hat{a}_{j,\tilde{\boldsymbol{q}}} \left|\Psi_0^N\right\rangle, \tag{5}$$

with $\hat{a}_{j,\tilde{\boldsymbol{q}}}$ annihilating an electron (creating a photo hole) in band j, and with crystal momentum $\tilde{\boldsymbol{q}}$, from the N-electron ground state $|\Psi_0^N\rangle$. Via this approximation, we neglect possible relaxations in the final $(N-1)$-electron system.

In the following, we take the m-th excited state with center-of-mass momentum $\boldsymbol{Q}$ as defined in Eq. (2) as the initial state, and assume that in the final state, the emitted electron has momentum $\boldsymbol{k}$, while the photo hole resides in $|\phi_{j,\tilde{\boldsymbol{q}}}\rangle$. Then, the matrix element $\langle\Psi_{\mathrm{f}}^N|\boldsymbol{A}\cdot\hat{\boldsymbol{P}}|\Psi_{\mathrm{i}}^N\rangle$ of Eq. (3) takes the form

$$M_{j,\tilde{\boldsymbol{q}},\boldsymbol{k}}^{(m,\boldsymbol{Q})}(\boldsymbol{A}) \equiv \left\langle \mathcal{A}\Psi_{j,\tilde{\boldsymbol{q}}}^{N-1}\gamma_{\boldsymbol{k}} \middle| \boldsymbol{A}\cdot\hat{\boldsymbol{P}} \middle| \Psi_{m,\boldsymbol{Q}}^N \right\rangle. \tag{6}$$

Note that with this matrix element, we can calculate the transition rate from $|\Psi_{m,\boldsymbol{Q}}^N\rangle$ to *one* specific final state $|\mathcal{A}\Psi_{j,\tilde{\boldsymbol{q}}}^{N-1}\gamma_{\boldsymbol{k}}\rangle$, where an electron has been removed from the j-th band (and carrying crystal momentum $\tilde{\boldsymbol{q}}$). To account for all possible photoemission final states, we will sum up the transition rates of all final hole quantum numbers at a later stage.

To proceed, we reduce the N-electron matrix element of Eq. (6) to an effective one-electron matrix element by introducing the Dyson orbital as the overlap between the initial N-electron and the final $(N-1)$-electron system [38,40,41]. In contrast to existing literature for isolated systems, we here perform this step for Bloch functions that carry an additional crystal momentum quantum number. We then get for the absolute of the matrix element

$$\left|M_{j,\tilde{\boldsymbol{q}},\boldsymbol{k}}^{(m,\boldsymbol{Q})}(\boldsymbol{A})\right| = \left| \int_V \mathrm{d}^3 r \gamma_{\boldsymbol{k}}^*(\boldsymbol{r}) \boldsymbol{A}\cdot\nabla D_{j,\tilde{\boldsymbol{q}}}^{(m,\boldsymbol{Q})}(\boldsymbol{r}) \right|, \tag{7}$$

where we have defined the effective single-particle Dyson wave function with Bloch momentum $\tilde{\boldsymbol{q}}$ as

$$D_{j,\tilde{\boldsymbol{q}}}^{(m,\boldsymbol{Q})}(\boldsymbol{r}) = \sqrt{N} \int_V \mathrm{d}^3 r_2 \ldots \mathrm{d}^3 r_N \Psi_{j,\tilde{\boldsymbol{q}}}^{N-1*}(\boldsymbol{r}_2, \ldots, \boldsymbol{r}_N) \times \Psi_{m,\boldsymbol{Q}}^N(\boldsymbol{r}, \boldsymbol{r}_2, \ldots, \boldsymbol{r}_N). \tag{8}$$

Here, the volume of integration V is the volume of the crystal, as defined by the unit cell and the sampling of the Brillouin zone in the periodic directions (using sufficient vacuum in the nonperiodic direction of the slab).

Next, we evaluate the formal definition of the Dyson wave function, starting from an alternative form, which employs the basis of valence- and conduction bands and is derived in Appendix A:

$$D_{j,\tilde{\boldsymbol{q}}}^{(m,\boldsymbol{Q})}(\boldsymbol{r}) = \sum_{v'} \sum_{\boldsymbol{q}'}^{\mathrm{BZ}} \left\langle \Psi_{j,\tilde{\boldsymbol{q}}}^{N-1} \middle| \hat{a}_{v',\boldsymbol{q}'} \middle| \Psi_{m,\boldsymbol{Q}}^N \right\rangle \phi_{v',\boldsymbol{q}'}(\boldsymbol{r}) + \sum_{c'} \sum_{\boldsymbol{q}'}^{\mathrm{BZ}} \left\langle \Psi_{j,\tilde{\boldsymbol{q}}}^{N-1} \middle| \hat{a}_{c',\boldsymbol{q}'} \middle| \Psi_{m,\boldsymbol{Q}}^N \right\rangle \xi_{c',\boldsymbol{q}'}(\boldsymbol{r}). \tag{9}$$

Inserting Eqs. (2) and (5), we get

$$\begin{aligned} D_{j,\tilde{\boldsymbol{q}}}^{(m,\boldsymbol{Q})}(\boldsymbol{r}) &= \sum_{v,v',c} \sum_{\boldsymbol{q},\boldsymbol{q}'}^{\mathrm{BZ}} X_{v,c,\boldsymbol{q}}^{(m,\boldsymbol{Q})} \left\langle \Psi_0^N \middle| \hat{a}_{j,\tilde{\boldsymbol{q}}}^\dagger \hat{a}_{v',\boldsymbol{q}'} \hat{a}_{c,\boldsymbol{q}+\boldsymbol{Q}}^\dagger \hat{a}_{v,\boldsymbol{q}} \middle| \Psi_0^N \right\rangle \phi_{v',\boldsymbol{q}'}(\boldsymbol{r}) \\ &\quad + \sum_{v,c,c'} \sum_{\boldsymbol{q},\boldsymbol{q}'}^{\mathrm{BZ}} X_{v,c,\boldsymbol{q}}^{(m,\boldsymbol{Q})} \left\langle \Psi_0^N \middle| \hat{a}_{j,\tilde{\boldsymbol{q}}}^\dagger \hat{a}_{c',\boldsymbol{q}'} \hat{a}_{c,\boldsymbol{q}+\boldsymbol{Q}}^\dagger \hat{a}_{v,\boldsymbol{q}} \middle| \Psi_0^N \right\rangle \xi_{c',\boldsymbol{q}'}(\boldsymbol{r}). \end{aligned} \tag{10}$$

For simplicity, we assume the ground state $|\Psi_0^N\rangle$ to be a single Slater determinant constructed from the Kohn-Sham valence orbitals $\phi_{v,\boldsymbol{q}}$. This allows us to work with the GW + BSE method carried out on top of density functional theory (DFT) calculations, but we note that the restriction to a single determinant also removes the anti-resonant (de-excitation) amplitudes of a beyond-Tamm-Dancoff solution, since these couple only to $(N-1)$-electron states of the form $\hat{a}_{c,\boldsymbol{q}}|\Psi_0^N\rangle$, which vanish for a single-determinant ground state. The first term in Eq. (10) containing the sum over v' then vanishes because the conduction electron created by $\hat{a}_{c,\boldsymbol{q}+\boldsymbol{Q}}^\dagger$ remains in the resulting determinant, which can therefore not coincide with $|\Psi_0^N\rangle$. Evaluating the one surviving contraction of the second term, $c' = c$, $v = j$, $\boldsymbol{q} = \tilde{\boldsymbol{q}}$, and $\boldsymbol{q}' = \boldsymbol{q} + \boldsymbol{Q}$, we thus find

$$D_{v,\boldsymbol{q}}^{(m,\boldsymbol{Q})}(\boldsymbol{r}) = \sum_c X_{v,c,\boldsymbol{q}}^{(m,\boldsymbol{Q})} \xi_{c,\boldsymbol{q}+\boldsymbol{Q}}(\boldsymbol{r}). \tag{11}$$

Inserting Eq. (11) into Eq. (7), we arrive at

$$\left|M_{v,\boldsymbol{q},\boldsymbol{k}}^{(m,\boldsymbol{Q})}(\boldsymbol{A})\right| = \left| \int_V \mathrm{d}^3 r \gamma_{\boldsymbol{k}}^*(\boldsymbol{r}) \boldsymbol{A}\cdot\nabla \sum_c X_{v,c,\boldsymbol{q}}^{(m,\boldsymbol{Q})} \xi_{c,\boldsymbol{q}+\boldsymbol{Q}}(\boldsymbol{r}) \right|. \tag{12}$$

To further evaluate the matrix element, we follow the commonly applied strategy in POT and approximate the photoelectron wave function by a plane-wave final state (PWFS): $\gamma_{\boldsymbol{k}}(\boldsymbol{r}) = e^{\mathrm{i}\boldsymbol{k}\cdot\boldsymbol{r}}/\sqrt{V}$. For static ARPES with photon energies of 15 to 50 eV, this simplifying assumption has been shown to yield photoelectron angular distributions in good agreement with experiment, not only for organic molecular layers [42–45], but also for 2D materials [46,47]. We expect a similar behavior for excited states [35]. It should be noted that for a such-defined final state, the surface-perpendicular component of the photoelectron's momentum k_z is given by its kinetic energy only; the PWFS assumption is thus not compatible with

a sampling of the BZ in this direction. This is not a restriction, since photoemission from solids in this probe-energy regime effectively always probes a surface and therefore breaks the periodicity in the surface-perpendicular direction. We also remark that it is customary in parts of the community to simulate ARPES from bulk systems by calculating the spectral function. If, however, matrix elements are to be taken into account, one must rather approach the bulk limit by taking multiple layers and an appropriate damping of the final state into account [48,49]. In principle, our approach can also be extended to more accurate descriptions of the photoelectron final state, such as the recently suggested ones based on the solution of the Lippmann-Schwinger equation [50], but this is beyond the scope of the present work. Inserting $\gamma_{\boldsymbol{k}}$ into Eq. (12), integrating by parts and dropping the surface term, allows us to furthermore write the matrix element as a sum over Fourier-transformed Bloch functions:

$$\left|M^{(m,\boldsymbol{Q})}_{v,\boldsymbol{q},\boldsymbol{k}}(\boldsymbol{A})\right| = \left|\frac{\boldsymbol{A}\cdot\boldsymbol{k}}{\sqrt{V}}\sum_{c} X^{(m,\boldsymbol{Q})}_{v,c,\boldsymbol{q}}\mathcal{F}[\xi_{c,\boldsymbol{q}+\boldsymbol{Q}}](\boldsymbol{k})\right|. \tag{13}$$

Before putting everything together, we also take the energy conservation defined in Eq. (3) into account. To this end, we identify the energy of the initial state as the sum of the ground state energy E^N_0 and the excitation energy $\Omega^{(m,\boldsymbol{Q})}$. The energy of the final state consists of the photoelectron kinetic energy $E_{\mathrm{kin}} = k^2/2$ and the energy of the $(N-1)$-electron state $E^{N-1}_{v,\boldsymbol{q}}$. The latter can be expressed as the ground-state energy plus the ionization energy of the v-th valence band at $\boldsymbol{q}$: $\varepsilon_{v,\boldsymbol{q}}$. This leads to

$$\delta(\omega + E_{\mathrm{i}} - E_{\mathrm{f}}) = \delta(\omega + \Omega^{(m,\boldsymbol{Q})} - \varepsilon_{v,\boldsymbol{q}} - E_{\mathrm{kin}}). \tag{14}$$

Combining this expression for the energy conservation with the matrix element of Eq. (13), we can now rewrite the transition rate W in Eq. (3). This rate gives the probability for the m-th exciton, with excitation energy $\Omega^{(m,\boldsymbol{Q})}$ and center-of-mass momentum $\boldsymbol{Q}$, to end up in a state with photoelectron momentum $\boldsymbol{k}$ if the photohole resides in valence orbital $\phi_{v,\boldsymbol{q}}$:

$$W_{(m,\boldsymbol{Q})\to(v,\boldsymbol{q},\boldsymbol{k})} = \frac{2\pi}{V}|\boldsymbol{A}\cdot\boldsymbol{k}|^2\left|\sum_{c} X^{(m,\boldsymbol{Q})}_{v,c,\boldsymbol{q}}\mathcal{F}[\xi_{c,\boldsymbol{q}+\boldsymbol{Q}}](\boldsymbol{k})\right|^2 \times \delta(\omega + \Omega^{(m,\boldsymbol{Q})} - \varepsilon_{v,\boldsymbol{q}} - E_{\mathrm{kin}}). \tag{15}$$

Summing up the transition rates for all final-state quantum numbers v and $\boldsymbol{q}$, we get an expression which is proportional to the overall photoelectron intensity,

$$I_{m,\boldsymbol{Q}}(\boldsymbol{k}) \propto |\boldsymbol{A}\cdot\boldsymbol{k}|^2\sum_{v}\sum_{\boldsymbol{q}}^{\mathrm{BZ}}\left|\sum_{c} X^{(m,\boldsymbol{Q})}_{v,c,\boldsymbol{q}}\mathcal{F}[\xi_{c,\boldsymbol{q}+\boldsymbol{Q}}](\boldsymbol{k})\right|^2 \times \delta(\omega + \Omega^{(m,\boldsymbol{Q})} - \varepsilon_{v,\boldsymbol{q}} - E_{\mathrm{kin}}), \tag{16}$$

where $I_{m,\boldsymbol{Q}}(\boldsymbol{k})$ denotes the number of photoelectrons of momentum $\boldsymbol{k}$ that are emitted from the m-th excited state carrying center-of-mass momentum $\boldsymbol{Q}$. Finally, if we want to simulate photoemission not only from a single pure state, but rather from an incoherent population of multiple exciton states, we can incoherently sum the contributing photoemission signals, that is, perform a sum $I(\boldsymbol{k}) = \sum_m \sum_{\boldsymbol{Q}} w_{m,\boldsymbol{Q}} I_{m,\boldsymbol{Q}}(\boldsymbol{k})$ with weights $w_{m,\boldsymbol{Q}}$. In turn, for a given experimental pump-probe photoemission signal, its composition in terms of pure exciton states can be determined.

In summary, photoemission from a static (or, in practice, long-lived, quasistatic) exciton state is given by a sum over crystal momentum and hole state contributions, for which the photoelectron kinetic energy is determined by the energy conservation between the probe-, pump-, and hole energy. At each allowed kinetic energy, the photoelectron angular distribution is given by the absolute square of a coherent sum over electron contributions, weighted by the respective electron-hole transition coefficients, which are obtained from the solutions of the BSE. In contrast to other formulations of exciton photoemission that only consider the spectral function [19,20], our formalism includes photoelectron matrix element effects due to the probe pulse and at the level of the PWFS approximation. For simplicity, we have restricted the derivation to systems with a closed-shell spin-singlet ground state, such that excitons are obtained as spin-singlets and spin-triplets [2,51]; we remark that an extension to a more general spin treatment in terms of spinors is straightforward.

B. Pump-induced effects on exciton photoemission

In the preceding derivation, we assumed the system to be in an *eigenstate* of the BSE Hamiltonian $|m,\boldsymbol{Q}\rangle$ whose real-space representation is given in Eq. (1). The resulting expression for the photoelectron intensity [Eq. (16)] applies to such an eigenstate and does not consider how the system was initially prepared by the pump pulse. In general, however, the pump pulse typically generates a *superposition* state—a linear combination of the calculated eigenstates—which necessitates an adaptation of our formalism, as detailed below. In preparation for Sec. III, we restrict the discussion to optical excitations ($\boldsymbol{Q}\to 0$), allowing us to denote the eigenstates of the BSE Hamiltonian as $|m,\boldsymbol{Q}=0\rangle =: |m\rangle$. The superposition state $|S_l\rangle$, created by the pump laser, then becomes

$$|S_l\rangle = \sum_m c^l_m |m\rangle. \tag{17}$$

As mentioned above, the presented formalism [Eq. (16)] is only suitable for photoemission from an eigenstate of the BSE Hamiltonian. Assuming that the superposition state $|S_l\rangle$ created by the pump field is a combination of energy-degenerate eigenstates (obtained from solving the BSE), it is itself an eigenstate of the BSE Hamiltonian, thus allowing us to still apply the formalism. Therefore, we define a small enough energy difference $\eta > 0$, which spans the degenerate subspace around excitation energy Ω_l, and get the expansion coefficients c^l_m, dependent on the polarization $\boldsymbol{E}$ of the pump pulse, via the optical transition matrix elements:

$$c^l_m \propto \langle m|\boldsymbol{E}\cdot\hat{\boldsymbol{P}}|0\rangle\ \mathbf{1}(|\Omega^{(m)} - \Omega_l| < \eta), \tag{18}$$

where $|0\rangle$ denotes the ground state and where the indicator function $\mathbf{1}()$ evaluates to 1 if its argument is true and else becomes 0. The transition matrix elements may alternatively be calculated based on the velocity operator for a more sophisticated treatment of the electron-photon interaction [2]. These velocity-based transition matrix elements are directly available in the BERKELEYGW code [1,2,52] and were used to form the superposition states throughout this text.

As a consequence, for photoemission intensity from the superposition (eigen)state $|S_l\rangle$, the transition density matrix elements are also linearly combined, and thus Eq. (16) must be modified accordingly ($\boldsymbol{Q} = 0$):

$$I_{S_l}(\boldsymbol{k}) \propto |\boldsymbol{A}\cdot\boldsymbol{k}|^2 \sum_v \sum_{\boldsymbol{q}}^{\mathrm{BZ}} \left| \sum_c \sum_m c_m^l X_{v,c,\boldsymbol{q}}^{(m)} \mathcal{F}[\xi_{c,\boldsymbol{q}}](\boldsymbol{k}) \right|^2 \times \delta(\omega + \Omega_l - \varepsilon_{v,\boldsymbol{q}} - E_{\mathrm{kin}}). \quad (19)$$

Note that the new transition density matrix $\sum_m c_m^l X_{v,c,\boldsymbol{q}}^{(m)}$ can readily be identified as the BSE eigenvector of the superposition state. The procedure presented in this section can thus also be understood as a simple basis change within the subspace of degenerate eigenstates, or, in other words, as a change from the basis obtained through solution of the BSE to a basis determined by the pump polarization.

In 2D systems, excitons typically occur as degenerate pairs, and only their superposition should be considered as the physical exciton, which then, for instance, also respects the symmetries of the system [53,54]. In contrast to those eigenstates, the pump pulse in general breaks the system's symmetry and may create superimposed exciton states that depend on the pump polarization. As we will show in Sec. III C, such pump polarization effects have a considerable imprint on exciton photoemission.

III. RESULTS

A. Calculation of hBN quasiparticle and optical properties

In the following, we exemplify our formalism by the simulation of excitonic photoemission in monolayer hexagonal boron nitride (hBN) as a prototypical 2D system. As a starting point, we obtain wave functions and energy levels from DFT calculations with QUANTUM ESPRESSO [55–57], using the PBE-GGA exchange-correlation functional [58] and a lattice constant of 2.507 Å; see Fig. 1(a). To compensate for the systematic underestimation of the band gap within semilocal DFT, we apply the G_0W_0 method to correct the energy levels. Utilizing the BERKELEYGW code [1,2,52], we obtain a direct (indirect) band gap of 7.7 eV (7.2 eV), which is comparable to literature values from similar methods; see, e.g., Ref. [59] for a comparison. We show the G_0W_0 band structure in Fig. 1(b) and detail the computational methods in Appendix C.

Subsequently, we use the DFT wave functions and G_0W_0 energy levels, and solve the BSE within the TDA and for $\boldsymbol{Q} = 0$. This yields the excitation energies Ω_m and the BSE eigenvectors $|m, \boldsymbol{Q} = 0\rangle \equiv |m\rangle$, which we use to simulate optical spectra (compare Ref. [2]). As shown in Fig. 2(a), the BSE spectrum features a range of excitonic peaks below the band gap. These are often interpreted as hydrogen-like solutions of the Wannier equation [60], though they have also been found to deviate from that model [53]. For comparison, we include the optical spectrum computed within the independent-particle approximation, shown as a dashed blue curve in Fig. 2(a). In the following, we focus on the two lowest excitons, located at 5.3 eV (S_1) and 6.2 eV (S_2).

Both S_1 and S_2 are composed of two degenerate eigenstates of the BSE Hamiltonian. This results in an additional

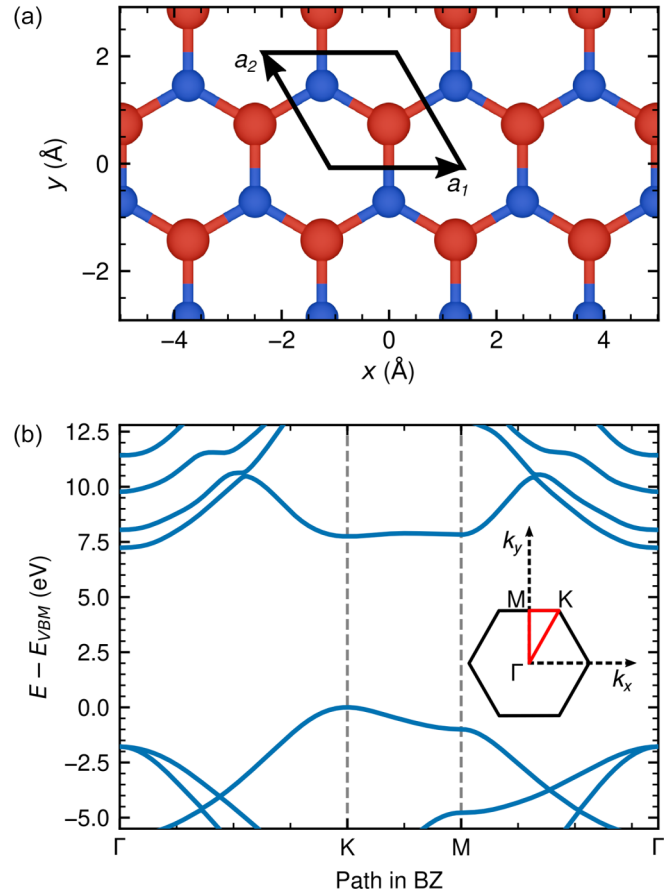


FIG. 1. (a) Atomic structure of hBN. Boron and nitrogen atoms are depicted in red and blue, respectively. The vectors $\mathbf{a_1}$ and $\mathbf{a_2}$ span the primitive unit cell, which contains one atom of each kind. (b) G_0W_0 band structure of hBN. Quasiparticle energies are shown along the $\Gamma - K - M - \Gamma$ high-symmetry path. The calculated band structure exhibits an indirect band gap, with the valence-band maximum and conduction-band minimum being located at K (and K') and Γ, respectively.

dependence on the pump polarization, as discussed in Sec. II B, and which will become relevant at a later stage in Sec. III C. For S_1 at 5.3 eV, the two degenerate valence-conduction transitions occur at K and K', respectively, with their momentum-dependent transition weights indicated in Fig. 2(b). The situation is similar for S_2 at 6.2 eV, albeit with transition weights being more spread out along the Brillouin-zone boundary, as can be seen in Fig. 2(c).

B. Exciton photoemission in hBN

With the quasiparticle and optical properties at hand, we now illustrate consequences of our theory for exciton photoemission from monolayer hBN. In the following, we use a 26.5 eV probe energy with a Gaussian energy broadening of 0.1 eV. For better insight into the pump-induced effects on the momentum maps, we ignore the trivial effect of probe polarization, stemming from the $|\boldsymbol{A}\cdot\boldsymbol{k}|^2$ prefactor in Eq. (16). Note that our formulation only considers excitonic photoemission, thereby neglecting photoemission from the initially populated electronic structure and associated effects like its

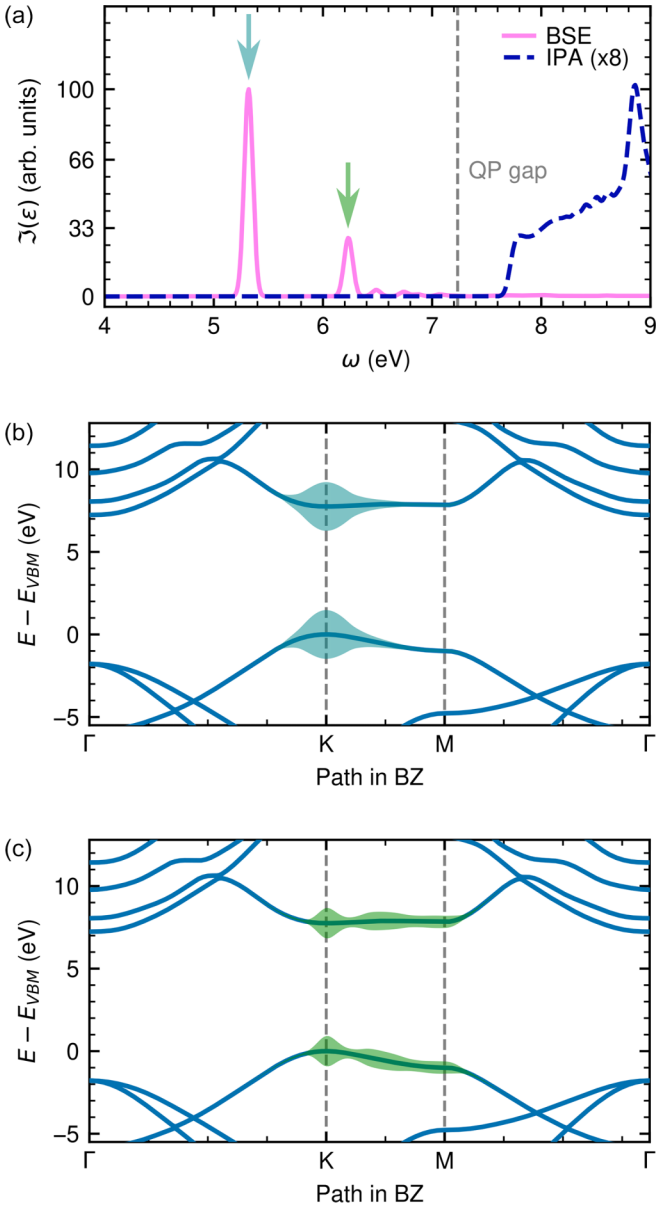


FIG. 2. Optical excitation of monolayer hBN. (a) Independent-particle spectrum, based on a G_0W_0 calculation in dark blue and the BSE spectrum in pink. In the latter, S_1 and S_2 energies are marked by arrows. Panels (b) and (c) show the G_0W_0 band structure with overlays indicating the BSE eigenvector composition of the S_1 (blue) and S_2 (green) excitations of the system, respectively.

depopulation due to exciton creation. This decoupling is a direct consequence of energy conservation in excitonic photoemission [Eq. (16)]. The exciton energy $\Omega^{(m,\boldsymbol{Q})}$ is transferred to the photoelectron, yielding higher kinetic energies than those obtained from photoemission out of the initially populated electronic states (see Fig. 3).

In Fig. 3, we show the simulated band map for photoemission from the S_1 exciton together with the G_0W_0 band structure (full blue lines) along the $\Gamma - K' - M_2$ path (corresponding to the k_x direction, see inset). According to Eq. (16), the energy dispersion of exciton photoemission is determined by the hole component of the exciton. Consequently, the exciton's trARPES signature appears at the photoelectron

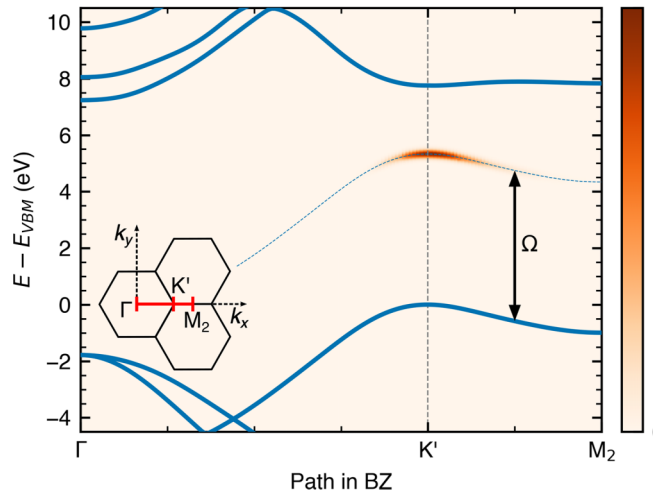


FIG. 3. ARPES band map for the S_1 exciton in k_x direction (cut of the BZ along $\Gamma - K' - M_2$, see inset with three neighboring BZs). The G_0W_0 band structure is overlaid in full blue lines, with a duplicate of the valence band, shifted by Ω, as a blue dashed line.

kinetic energy corresponding to the valence band energy plus the pump energy Ω (blue dashed line). This finding, which is well-established in the literature [19,61], enables the estimation of the exciton's spatial extent from photoemission data under the assumption of an *s*-like envelope function [4,5,62].

Next, it is expedient to compare momentum maps of exciton photoemission with those for photoemission from the ground state, which we obtain by the standard way of simulating POT [48]. In Fig. 4(a), we present such a map for a kinetic energy slightly below the valence band maximum (VBM) ($E - E_{\mathrm{VBM}} = -0.2$ eV), which is comprised of six triangular features, each around the K/K' points. This pattern is analogous to the case of graphene, where the triangular features are also broken in the outgoing direction of the Brillouin zone, leading to croissant- or horseshoe-like shapes. This "dark corridor" is due to matrix element effects in the photoemission process and has already been described in great detail for the case of graphene [14,63,64]. When assuming a static population of the conduction band, the latter would also be accessible to photoemission from the ground state, which we simulate in panel (b) of Fig. 4, using a kinetic energy of 26.6 eV, which is above the conduction band minimum

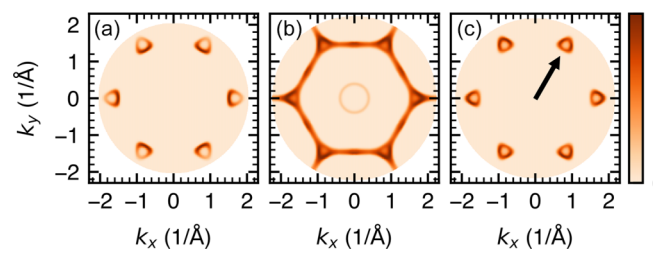


FIG. 4. Momentum maps for three different cases: (a) valence band at $E - E_{\mathrm{VBM}} = -0.2$ eV ($E_{\mathrm{kin}} = 18.6$ eV), (b) conduction band at $E - E_{\mathrm{CBM}} = +0.6$ eV ($E_{\mathrm{kin}} = 26.6$ eV), and (c) S_1 exciton at $E - E_{\mathrm{VBM}} = \Omega - 0.2$ eV ($E_{\mathrm{kin}} = 23.9$ eV).

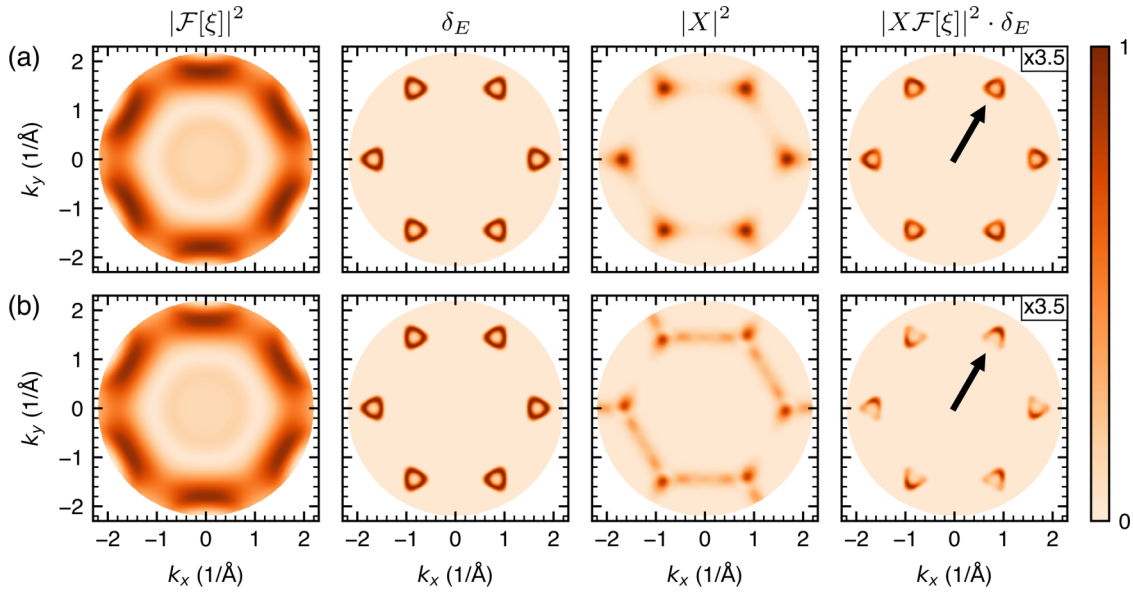


FIG. 5. Decomposition of exciton ARPES maps for S_1 in row (a) and S_2 in row (b), with black arrows indicating the polarization of the pump laser. First column: Fourier-transformed conduction-band wave functions. Second column: energy-conservation delta function. Third column: BSE eigenvectors. Fourth column: resulting exciton ARPES maps as products of the first to third columns. Each map is individually normalized to one. For S_1 in row (a), the horseshoes point away from Γ, with minor modulations along their contours. For S_2 in row (b), four of the six horseshoes are rotated when compared to the first exciton. This is a direct result of the differences in the momentum-space distribution of their BSE eigenvectors.

(CBM) ($E - E_{\mathrm{CBM}} = +0.6$ eV). Note that this is a hypothetical example for illustration purposes; in an actual experiment, this would correspond to the situation where a formerly unoccupied state gets populated by, e.g., a charge-transfer process across an interface. In contrast to the valence band case depicted in panel (a), the features around the Dirac point are now elongated in the directions going to the M/M' points, which is reasonable when looking at the band structure (see, e.g., Fig. 1). Remarkably, the dark corridor from the matrix element effect is now pointing to the *inside* of the BZ. Returning now to the simulation of exciton photoemission, we show a momentum map of the S_1 exciton in Fig. 4(c), using a kinetic energy of 23.9 eV and a pump polarization, as indicated by a black arrow. As already discussed in the preceding paragraph, the exciton inherits the energy dispersion of the *hole* (here, the highest valence band), but, in light of Eq. (16), follows the momentum distribution given by the Fourier-transformed *electron* part of the exciton wave function (here, the lowest conduction band). As a direct imprint of the latter, the dark corridor is also pointing to the inside of the BZ, which we can see clearly in Fig. 4(c). Having established the unoccupied part of the electronic structure as another direct marker of exciton photoemission, we will now examine the different contributions to the momentum maps in more detail.

Using Eq. (16), we dissect the photoemission maps for both excitons, S_1 and S_2, in order to understand the influence of each contributing factor. Since—in this case—both excitons only involve transitions from the highest valence to the lowest conduction band, the sums over v and c in Eq. (16) collapse. Consequently, we are left with a single product of $|\mathcal{F}[\xi]|^2$, δ_E, and $|X|^2$, involving only wave functions from the lowest conduction band, energies of the highest valence band, and BSE transition coefficients from the highest valence band to the lowest conduction band. Figure 5 shows these three factors, as well as the full photoemission maps, for the two excitons in row (a) (S_1) and row (b) (S_2), respectively. The direction of the pump polarization is indicated in the rightmost column. For both excitons S_1 and S_2, the triangular patterns are generated by the δ_E factor, with $|\mathcal{F}[\xi]|^2$ only leading to slight modifications. The maps in the first two columns, $|\mathcal{F}[\xi]|^2$ and δ_E, are very similar between the two excitons, S_1 and S_2, with minor differences arising due to the unequal photoelectron kinetic energies (23.9 eV for S_1 and 24.8 eV for S_2). Since all other areas already have vanishing intensity, the additional multiplication with the BSE eigenvector can at most lead to intensity differences within the area of the horseshoes. As can be seen from the third column, the BSE eigenvectors of the two excitons differ, leading to the differences in their respective photoemission maps (rightmost column of Fig. 5). In the following, those differences are inspected more closely.

For S_1, the BSE eigenvector [third column in Fig. 5(a)] mostly exhibits a sixfold symmetry. It is centered around the K and K' points and varies weakly along the contours of the horseshoes, thus leading only to small intensity variations [fourth column in Fig. 5(a)] along them. Contrary, in the case of S_2 in row (b), the BSE eigenvector exhibits a nodal line perpendicular to the pump polarization—which has broken the sixfold symmetry—while being nonzero along the remaining four sides of the hexagonal BZ. Since the pump polarization was chosen along a high-symmetry direction (indicated by black arrows in the rightmost column), it acts as a symmetry axis for the BSE eigenvector and, consequently, for the resulting photoemission map. In contrast to the case of S_1, the regions around K and K' show much more detail for S_2, particularly featuring small nodal lines, which, upon multiplication of the BSE eigenvector with the horseshoe

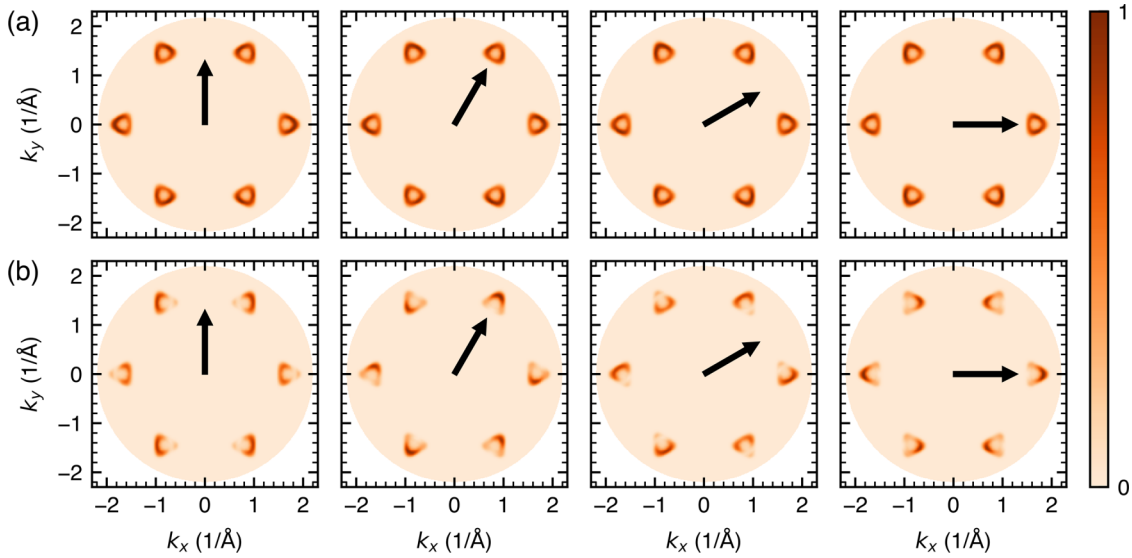


FIG. 6. Influence of pump laser's polarization on exciton photoemission. The four columns show ARPES photoemission maps for different polarizations of the pump laser (black arrows). (a) shows photoemission from the lowest-energy exciton, while (b) shows the second exciton. In the case of the first exciton, only small differences in the intensity distribution along the horseshoes are visible, while for the second exciton, there is a strong dependence on the pump polarization, with different polarizations leading to different rotations of the horseshoes. In the case of both excitons, the photoemission maps are mirror symmetric across the (high-symmetry) polarization directions.

pattern produced by $|\mathcal{F}[\xi]|^2$ and δ_E, suppress photoemission intensity. Moreover, the local maxima are shifted off K and K'. As can be seen in the last column of Fig. 5, the combination of all three factors effectively leads to a redistribution of spectral intensity within the horseshoes. By selectively accessing the different factors in Eq. (16), we are thus able to deconvolute different contributions to the momentum maps. In the general case of multiple transitions within an exciton, however, the sums over different valence and conduction bands remain and, as a result, the above analysis would become less straightforward, especially due to the coherent summation of the electron part. Since in the present case of the hBN example we found the most asymmetry to arise due to the BSE eigenvectors in conjunction with the pump polarization, we will discuss this effect in more detail in the following.

C. Pump polarization effects in 2D hBN

As outlined in Sec. II B, the summation of energy-degenerate BSE eigenvectors, in order to form a superimposed exciton, involves coefficients that depend on the polarization of the pump pulse. The influence of pump polarization is illustrated in detail in Fig. 6. Panels (a) and (b) of Fig. 6 depict the photoemission from the S_1 exciton (5.3 eV) at a kinetic energy of 23.9 eV and the S_2 exciton (6.2 eV) at 24.8 eV, respectively. The black arrows indicate the polarization direction of the pump pulse. Photoemission from the first exciton is only weakly dependent on the pump pulse's polarization and retains the horseshoe intensity pattern. Varying the polarization reveals minor variations in the intensity distributions along the horseshoes. For the second exciton, however, there is a strong dependence of the photoemission intensity distribution on the pump pulse, where different polarization directions lead to different redistributions of spectral weight within the horseshoes. Although the probe pulse polarization may introduce an overall attenuation in a trARPES experiment, pump-induced effects on exciton photoemission are therefore expected to be observable, provided that sufficient energy and momentum resolution are achieved.

We close this section by making the experimental requirements for observing the predicted signatures explicit. Our formalism describes photoemission from a pure exciton state and therefore applies to a pump-probe delay that is longer than the dephasing of the optically induced polarization, but shorter than the lifetime of the exciton population. Moreover, the energy and momentum resolution must be sufficient to separate the excitonic species of interest, both from the remaining exciton manifold and from the photoemission signal of the occupied ground-state electronic structure. While these conditions are demanding, they are within reach of current experiments: time resolutions of several tens of femtoseconds are achieved in modern time- and momentum-resolved photoemission [65]. Such fine resolution has already allowed us to follow the dynamics of short-lived excitonic states [66], and both dephasing and population relaxation times can exceed 100 fs in 2D materials, in particular at low temperatures [67]. Likewise, such energy and momentum resolution allows us to distinguish different excitonic species in monolayer semiconductors [4,6], and their energetic separation could, to some extent, be tuned externally, for instance by strain or magnetic fields. The situation is naturally less favorable for higher-lying states, such as the S_2 exciton discussed above, and for materials hosting a dense manifold of excitons formed from different valleys. We stress, however, that a spectral overlap of several species does not invalidate the analysis: as discussed at the end of Sec. II, the measured intensity is then given by an incoherent sum over the contributing exciton states, each of which carries its own characteristic momentum fingerprint, so that the composition of the excited-state population remains

accessible through a comparison with simulated momentum maps. The feasibility of such an analysis has recently been demonstrated for excitons in an organic semiconductor, where time-resolved photoemission orbital tomography was used to image the momentum-space distribution of the exciton wave function and its time evolution [35].

IV. CONCLUSIONS

We have developed a framework for exciton photoemission orbital tomography (exPOT) in periodic systems, thereby enabling the computation and interpretation of photoemission angular distributions from excitons in two-dimensional materials and surfaces of crystalline solids. The exPOT formalism is derived from first principles, using many-body perturbation theory and the Dyson orbital concept, and connects the photoemission intensity to results from $GW+$ Bethe-Salpeter calculations. As a manifestation of the electron-hole correlation, for each hole configuration, exciton photoemission is expressed as a coherent sum over Fourier-transformed conduction-band wave functions, weighted by the Bethe-Salpeter eigenvector components.

We have implemented the formalism in a computational workflow compatible with standard plane-wave basis set $GW+$BSE, using DFT wave functions, GW energies, and BSE eigenvectors. As a proof of concept, we have applied our formalism to the prototypical case of monolayer hexagonal boron nitride. The resulting exPOT maps exhibit distinct patterns for different excitonic states. These patterns are characterized by an energy dispersion that follows the hole states, while the electron part of the exciton wave function is reflected in the photoemission matrix element. Both contributions are further modified by the BSE eigenvectors. The latter introduces an additional dependence on the pump polarization, resulting in the suppression of spectral weight in the momentum maps as a direct consequence of the excitonic character.

The exPOT formalism for periodic systems provides a powerful tool for gaining microscopic insight into the internal structure of excitons and offers a predictive framework for designing and interpreting next-generation trARPES experiments on quantum materials. Our formalism also includes excitons with finite center-of-mass momentum, making it particularly suited for elucidating the nature of momentum-dark excitons by bridging the gap between *ab initio* many-body theory and experimentally measurable momentum-resolved spectra.

ACKNOWLEDGMENTS

We acknowledge support from the European Research Council under the Synergy Grant "Orbital Cinema", Project ID No. 101071259. The computational results have been achieved using the Austrian Scientific Computing infrastructure and on Leonardo at CINECA, Italy, under the EuroHPC award with Project ID No. EHPC-EXT-2024E02-054. The authors acknowledge the financial support of the University of Graz.

DATA AVAILABILITY

All input and output files necessary to reproduce the computational data generated in this study are publicly available [68].

APPENDIX A: EXPANSION OF DYSON ORBITALS IN BLOCH STATES

In this section, we derive the expansion [Eq. (9)] of the Dyson orbitals, as given in Eq. (8), in terms of Bloch functions.

Since this expansion holds in general, we start with the Dyson orbital formed by the overlap of an arbitrary $(N-1)$- and N-electron wave function:

$$D(\boldsymbol{r}) = \sqrt{N}\int_V \mathrm{d}^3 r_2 \ldots \mathrm{d}^3 r_N \Psi^{N-1}(\boldsymbol{r}_2, \ldots, \boldsymbol{r}_N)^* \Psi^N(\boldsymbol{r}, \boldsymbol{r}_2, \ldots, \boldsymbol{r}_N). \tag{A1}$$

Next, since the Dyson orbitals are one-electron wave functions, they can be expanded in any set of one-electron basis functions. For a set of (Born-von Kármán-periodic, BvK-periodic, just like D) orthonormal basis functions $\{\psi_j(\cdot)\}$, we can thus write

$$D(\boldsymbol{r}) = \sum_j c_j \psi_j(\boldsymbol{r}), \tag{A2}$$

with linear coefficients

$$c_j = \int_V \mathrm{d}^3 r \psi_j(\boldsymbol{r})^* D(\boldsymbol{r}), \tag{A3}$$

where V is the crystal volume; see text below Eq. (8). Inserting the Dyson orbital and renaming $\boldsymbol{r}$ to $\boldsymbol{r}_1$, we get

$$c_j = \sqrt{N}\int_V \mathrm{d}^3 r_1 \mathrm{d}^3 r_2 \ldots \mathrm{d}^3 r_N \psi_j(\boldsymbol{r}_1)^* \Psi^{N-1}(\boldsymbol{r}_2, \ldots, \boldsymbol{r}_N)^* \Psi^N(\boldsymbol{r}_1, \boldsymbol{r}_2, \ldots, \boldsymbol{r}_N). \tag{A4}$$

Next, we rename $\boldsymbol{r}_1$ to $\boldsymbol{r}_2$ and vice versa to get

$$\begin{aligned} c_j &= \sqrt{N}\int_V \mathrm{d}^3 r_1 \mathrm{d}^3 r_2 \ldots \mathrm{d}^3 r_N \psi_j(\boldsymbol{r}_2)^* \Psi^{N-1}(\boldsymbol{r}_1, \boldsymbol{r}_3, \ldots, \boldsymbol{r}_N)^* \Psi^N(\boldsymbol{r}_2, \boldsymbol{r}_1, \ldots, \boldsymbol{r}_N) \\ &= \sqrt{N}\int_V \mathrm{d}^3 r_1 \mathrm{d}^3 r_2 \ldots \mathrm{d}^3 r_N \psi_j(\boldsymbol{r}_2)^* \Psi^{N-1}(\boldsymbol{r}_1, \boldsymbol{r}_3, \ldots, \boldsymbol{r}_N)^* (-\Psi^N(\boldsymbol{r}_1, \boldsymbol{r}_2, \ldots, \boldsymbol{r}_N)), \end{aligned} \tag{A5}$$

where we used the antisymmetry of the wave function in the last step. Using the same argument, we find for any i in $\{1, \ldots, N\}$,

$$c_j = \sqrt{N}\int_V \mathrm{d}^3 r_1 \ldots \mathrm{d}^3 r_N (-1)^{1+i} \psi_j(\boldsymbol{r}_i)^* \Psi^{N-1}(\boldsymbol{r}_1, \ldots, \boldsymbol{r}_{i-1}, \boldsymbol{r}_{i+1}, \ldots, \boldsymbol{r}_N)^* \Psi^N(\boldsymbol{r}_1, \boldsymbol{r}_2, \ldots, \boldsymbol{r}_N). \tag{A6}$$

We can thus write c_j as a sum over i as

$$c_j = \frac{1}{N}\sum_{i=1}^{N}\sqrt{N}\int_V \mathrm{d}^3r_1...\mathrm{d}^3r_N(-1)^{1+i}\psi_j(\boldsymbol{r}_i)^*\Psi^{N-1}(\boldsymbol{r}_1,\ldots,\boldsymbol{r}_{i-1},\boldsymbol{r}_{i+1},\ldots,\boldsymbol{r}_N)^*\Psi^N(\boldsymbol{r}_1,\ldots,\boldsymbol{r}_N)$$

$$= \int_V \mathrm{d}^3r_1...\mathrm{d}^3r_N\Psi^N(\boldsymbol{r}_1,\ldots,\boldsymbol{r}_N)\cdot\left(\sum_{i=1}^{N}\frac{(-1)^{1+i}}{\sqrt{N}}\psi_j(\boldsymbol{r}_i)\Psi^{N-1}(\boldsymbol{r}_1,\ldots,\boldsymbol{r}_{i-1},\boldsymbol{r}_{i+1},\ldots,\boldsymbol{r}_N)\right)^*. \tag{A7}$$

Now we can identify the expression in parentheses with the wave function of the antisymmetrized product state $|\mathcal{A}\psi_j\Psi^{N-1}\rangle$ (see, e.g., Ref. [38]). Using the creation operator $\hat{a}_j^\dagger$ corresponding to $|\psi_j\rangle$ and a bra-ket notation, we can thus write

$$c_j = \frac{1}{N!}\int_V \mathrm{d}^3r_1...\mathrm{d}^3r_N\langle\boldsymbol{r}_1,\ldots,\boldsymbol{r}_N|\Psi^N\rangle(\langle\boldsymbol{r}_1,\ldots,\boldsymbol{r}_N|\hat{a}_j^\dagger|\Psi^{N-1}\rangle)^*$$

$$= \frac{1}{N!}\int_V \mathrm{d}^3r_1...\mathrm{d}^3r_N\langle\Psi^{N-1}|\hat{a}_j|\boldsymbol{r}_1,\ldots,\boldsymbol{r}_N\rangle\langle\boldsymbol{r}_1,\ldots,\boldsymbol{r}_N|\Psi^N\rangle. \tag{A8}$$

Finally, we want to arrive at a basis-independent representation of c_j, which allows for efficient handling of the ladder-operator matrix elements. To do so, we make use of the fact that for every wave function $\Psi(\cdot)$ that satisfies BvK periodic boundary conditions for a large crystal, there is a nonperiodic wave function $\tilde{\Psi}(\cdot)$ that is equal to $\Psi(\cdot)$ inside the crystal, but vanishes quickly outside of the crystal. Then, we get

$$c_j = \frac{1}{N!}\int_V \mathrm{d}^3r_1...\mathrm{d}^3r_N\langle\Psi^{N-1}|\hat{a}_j|\boldsymbol{r}_1,\ldots,\boldsymbol{r}_N\rangle\langle\boldsymbol{r}_1,\ldots,\boldsymbol{r}_N|\Psi^N\rangle$$

$$\approx \frac{1}{N!}\int_V \mathrm{d}^3r_1...\mathrm{d}^3r_N\langle\tilde{\Psi}^{N-1}|\hat{\tilde{a}}_j|\boldsymbol{r}_1,\ldots,\boldsymbol{r}_N\rangle\langle\boldsymbol{r}_1,\ldots,\boldsymbol{r}_N|\tilde{\Psi}^N\rangle, \tag{A9}$$

where $\hat{\tilde{a}}_j$ is the destruction operator for $|\tilde{\psi}_j\rangle$, which is the nonperiodic equivalent of basis vector $|\psi_j\rangle$. Assuming the nonperiodic functions vanish quickly outside of V, we then get

$$c_j \approx \frac{1}{N!}\int_{\mathbb{R}^3} \mathrm{d}^3r_1...\mathrm{d}^3r_N\langle\tilde{\Psi}^{N-1}|\hat{a}_j|\mathbf{r}_1,\ldots,\mathbf{r}_N\rangle\langle\mathbf{r}_1,\ldots,\mathbf{r}_N|\tilde{\Psi}^N\rangle$$

$$= \langle\tilde{\Psi}^{N-1}|\hat{a}_j|\tilde{\Psi}^N\rangle, \tag{A10}$$

where we used

$$\hat{\mathbb{1}} = \frac{1}{N!}\int_{\mathbb{R}^3}\mathrm{d}^3r_1...\mathrm{d}^3r_N|\boldsymbol{r}_1,\ldots,\boldsymbol{r}_N\rangle\langle\boldsymbol{r}_1,\ldots,\boldsymbol{r}_N|. \tag{A11}$$

We can thus perform operations in a basis-independent manner using the nonperiodic wave functions and then transform back to the BvK wave functions. Symbolically, we can thus write

$$c_j = \langle\Psi^{N-1}|\hat{a}_j|\Psi^N\rangle, \tag{A12}$$

as a shorthand for the above-shown steps.

Inserting this into Eq. (A2), we get our final result for the expansion of the Dyson orbital D in an arbitrary, orthonormal basis set $\{\psi_j(\cdot)\}$:

$$D(\boldsymbol{r}) = \sum_j\langle\Psi^{N-1}|\hat{a}_j|\Psi^N\rangle\psi_j(\boldsymbol{r}). \tag{A13}$$

To get to Eq. (9), we then simply use the Bloch functions as basis functions and split the sum over bands into a sum over valence bands and a sum over conduction bands.

APPENDIX B: IMPLEMENTATION DETAILS

This section provides Eq. (16) in an alternative form that allows for efficient implementation when using a plane-wave basis set. We begin by expanding $\xi_{c,\boldsymbol{q}+\boldsymbol{Q}}(\boldsymbol{r})$ in a plane-wave basis (using Born-von Kármán, BvK, periodic boundary conditions):

$$\xi_{c,\boldsymbol{q}+\boldsymbol{Q}}(\boldsymbol{r}) = \frac{1}{V}\sum_{\boldsymbol{G}}c_{c,\boldsymbol{q}+\boldsymbol{Q}}(\boldsymbol{G})e^{\mathrm{i}(\boldsymbol{q}+\boldsymbol{Q}+\boldsymbol{G})\cdot\boldsymbol{r}},$$

$$c_{c,\boldsymbol{q}+\boldsymbol{Q}}(\boldsymbol{G}) = \int_V \mathrm{d}^3r\,\xi_{c,\boldsymbol{q}+\boldsymbol{Q}}(\boldsymbol{r})e^{-\mathrm{i}(\boldsymbol{q}+\boldsymbol{Q}+\boldsymbol{G})\cdot\boldsymbol{r}}. \tag{B1}$$

When restricting $\boldsymbol{k}$ to values for which $e^{\mathrm{i}\boldsymbol{k}\cdot\boldsymbol{r}}$ satisfies BvK boundary conditions over V, the Fourier transform

$$\mathcal{F}[\xi_{c,\boldsymbol{q}+\boldsymbol{Q}}](\boldsymbol{k}) = \int_V \mathrm{d}^3r\,\xi_{c,\boldsymbol{q}+\boldsymbol{Q}}(\boldsymbol{r})e^{-\mathrm{i}\boldsymbol{k}\cdot\boldsymbol{r}}, \tag{B2}$$

vanishes unless $\boldsymbol{q}+\boldsymbol{G}+\boldsymbol{Q}=\boldsymbol{k}$ for at least one of the reciprocal lattice vectors $\boldsymbol{G}$. Now, since $\boldsymbol{q}$ is restricted to the Brillouin zone (BZ), and $\boldsymbol{G}$ is a reciprocal lattice vector, there is only a single combination of $\boldsymbol{q}$ and $\boldsymbol{G}$ that satisfies this condition. Thus, the BZ summation is reduced to a single contributing $\boldsymbol{q}$ vector and

$$\mathcal{F}[\xi_{c,\boldsymbol{q}+\boldsymbol{Q}}](\boldsymbol{k}) = \sum_{\boldsymbol{G}}c_{c,\boldsymbol{q}+\boldsymbol{Q}}(\boldsymbol{G})\delta_{\boldsymbol{q}+\boldsymbol{G}+\boldsymbol{Q},\boldsymbol{k}}. \tag{B3}$$

The photoemission intensity may then be written as

$$I_{m,\boldsymbol{Q}}(\boldsymbol{k}) \propto |\boldsymbol{A}\cdot\boldsymbol{k}|^2 \sum_{v} \sum_{\boldsymbol{q}}^{\mathrm{BZ}} \sum_{\boldsymbol{G}} \delta_{\boldsymbol{q}+\boldsymbol{G}+\boldsymbol{Q},\boldsymbol{k}} \times \left| \sum_{c} X^{(m,\boldsymbol{Q})}_{v,c,\boldsymbol{q}} c_{c,\boldsymbol{q}+\boldsymbol{Q}}(\boldsymbol{G}) \right|^2 \delta(\omega + \Omega^{(m,\boldsymbol{Q})} - \varepsilon_{v,\boldsymbol{q}} - E_{\mathrm{kin}}). \tag{B4}$$

This can be used for an efficient implementation of the presented formalism: The grid of $\boldsymbol{G}$ vectors, determined by the used unit cell, and the grid of $\boldsymbol{q}$ vectors, determined by the used BZ sampling, create a grid of $\boldsymbol{k}$ vectors, $\boldsymbol{k} = \boldsymbol{q} + \boldsymbol{G} + \boldsymbol{Q}$, for which we get

$$I_{m,\boldsymbol{Q}}(\boldsymbol{k}) \propto |\boldsymbol{A}\cdot\boldsymbol{k}|^2 \sum_{v} \left| \sum_{c} X^{(m,\boldsymbol{Q})}_{v,c,\boldsymbol{q}} c_{c,\boldsymbol{q}+\boldsymbol{Q}}(\boldsymbol{G}) \right|^2 \times \delta(\omega + \Omega^{(m,\boldsymbol{Q})} - \varepsilon_{v,\boldsymbol{q}} - E_{\mathrm{kin}}), \quad \text{with } \boldsymbol{q}+\boldsymbol{G}+\boldsymbol{Q} = \boldsymbol{k}. \tag{B5}$$

For any photoelectron momentum $\boldsymbol{k}$ on this grid, we can thus directly use the plane-wave coefficients $c_{c,\boldsymbol{q}+\boldsymbol{Q}}(\boldsymbol{G})$, BSE eigenvector components $X^{(m,\boldsymbol{Q})}_{v,c,\boldsymbol{q}}$ and GW energies $-\varepsilon_{v,\boldsymbol{q}}$ (which are the negative of the ionization energies) to obtain the photoemission intensity $I_{m,\boldsymbol{Q}}(\boldsymbol{k})$, without the need for a BZ summation over $\boldsymbol{q}$. Given a sufficiently fine BZ sampling, the photoemission intensity for any $\boldsymbol{k}$ not on this grid (but within range of the energy cutoff used for wave functions in the DFT calculation) can then be obtained using efficient interpolation techniques.

APPENDIX C: COMPUTATIONAL DETAILS

For the example of monolayer hBN, we calculate Kohn-Sham DFT wave functions and energies in QUANTUM ESPRESSO [55–57] using the Perdew-Burke-Ernzerhof exchange-correlation functional, ONCV pseudopotentials, and a cutoff energy of 50 Ry and 200 Ry for the wave functions and the representation of the density, respectively. The lattice constant was set to 2.507 Å (bulk experimental value: 2.506 Å [69]), and we used a vacuum layer of 20 Å, as well as a truncation of the Coulomb interaction in the z direction [70], to avoid spurious interaction between repeated slabs from the periodic boundary condition. Based on these ground-state properties, we perform a G_0W_0 calculation using BERKELEYGW [1,2,52]. For the G_0W_0 calculation as well as for all other BERKELEYGW calculations, we use the slab truncation scheme [52]. In particular, we use the *NNS* subsampling technique, which, for systems with reduced dimensionality, accelerates convergence with respect to the Brillouin-zone sampling [71]. For the calculation of the static inverse dielectric function, we use a $12 \times 12 \times 1$ sampling of the Brillouin zone, a cutoff energy of 30 Ry for reciprocal lattice vectors, and sum over 200 bands. Based on this, we calculate the G_0W_0 energies for four valence and 44 conduction bands, using the same k-space mesh and reciprocal lattice cutoff as for the inverse dielectric function.

Finally, we construct the BSE Hamiltonian using four valence and nine conduction bands on a $12 \times 12 \times 1$ k-space mesh, interpolate it to a $96 \times 96 \times 1$ k-space mesh (four valence, four conduction bands) and diagonalize it.

[1] M. S. Hybertsen and S. G. Louie, Electron correlation in semiconductors and insulators: Band gaps and quasiparticle energies, Phys. Rev. B **34**, 5390 (1986).

[2] M. Rohlfing and S. G. Louie, Electron-hole excitations and optical spectra from first principles, Phys. Rev. B **62**, 4927 (2000).

[3] G. Onida, L. Reining, and A. Rubio, Electronic excitations: Density-functional versus many-body Green's-function approaches, Rev. Mod. Phys. **74**, 601 (2002).

[4] J. Madéo, M. K. L. Man, C. Sahoo, M. Campbell, V. Pareek, E. L. Wong, A. Al-Mahboob, N. S. Chan, A. Karmakar, B. M. K. Mariserla, X. Li, T. F. Heinz, T. Cao, and K. M. Dani, Directly visualizing the momentum-forbidden dark excitons and their dynamics in atomically thin semiconductors, Science **370**, 1199 (2020).

[5] M. K. L. Man, J. Madéo, C. Sahoo, K. Xie, M. Campbell, V. Pareek, A. Karmakar, E. L. Wong, A. Al-Mahboob, N. S. Chan, D. R. Bacon, X. Zhu, M. M. M. Abdelrasoul, X. Li, T. F. Heinz, F. H. da Jornada, T. Cao, and K. M. Dani, Experimental measurement of the intrinsic excitonic wave function, Sci. Adv. **7**, eabg0192 (2021).

[6] S. Dong, M. Puppin, T. Pincelli, S. Beaulieu, D. Christiansen, H. Hübener, C. W. Nicholson, R. P. Xian, M. Dendzik, Y. Deng, Y. W. Windsor, M. Selig, E. Malic, A. Rubio, A. Knorr, M. Wolf, L. Rettig, and R. Ernstorfer, Direct measurement of key exciton properties: Energy, dynamics, and spatial distribution of the wave function, Nat. Sci. **1**, e10010 (2021).

[7] R. Wallauer, M. Raths, K. Stallberg, L. Münster, D. Brandstetter, X. Yang, J. Güdde, P. Puschnig, S. Soubatch, C. Kumpf, F. C. Bocquet, F. S. Tautz, and U. Höfer, Tracing orbital images on ultrafast time scales, Science **371**, 1056 (2021).

[8] R. Wallauer, R. Perea-Causin, L. Münster, S. Zajusch, S. Brem, J. Güdde, K. Tanimura, K.-Q. Lin, R. Huber, E. Malic, and U. Höfer, Momentum-resolved observation of exciton formation dynamics in monolayer WS_2, Nano Lett. **21**, 5867 (2021).

[9] W. Bennecke, A. Windischbacher, D. Schmitt, J. P. Bange, R. Hemm, C. S. Kern, G. D'Avino, X. Blase, D. Steil, S. Steil, M. Aeschlimann, B. Stadtmüller, M. Reutzel, P. Puschnig, G. S. M. Jansen, and S. Mathias, Disentangling the multiorbital contributions of excitons by photoemission exciton tomography, Nat. Commun. **15**, 1804 (2024).

[10] M. Reutzel, G. S. M. Jansen, and S. Mathias, Probing excitons with time-resolved momentum microscopy, Adv. Phys.: X **9**, 2378722 (2024).

[11] M. Dauth and S. Kümmel, Predicting photoemission intensities and angular distributions with real-time density-functional theory, Phys. Rev. A **93**, 022502 (2016).

[12] U. De Giovannini, H. Hübener, and A. Rubio, A first-principles time-dependent density functional theory framework for spin and time-resolved angular-resolved photoelectron spectroscopy in periodic systems, J. Chem. Theory Comput. **13**, 265 (2017).

[13] M. Dauth, M. Graus, I. Schelter, M. Wießner, A. Schöll, F. Reinert, and S. Kümmel, Perpendicular emission, dichroism, and energy dependence in angle-resolved photoemission: The importance of the final state, Phys. Rev. Lett. **117**, 183001 (2016).

[14] C. S. Kern, A. Haags, L. Egger, X. Yang, H. Kirschner, S. Wolff, T. Seyller, A. Gottwald, M. Richter, U. De Giovannini, A. Rubio, M. G. Ramsey, F. C. Bocquet, S. Soubatch, F. S. Tautz, P. Puschnig, and S. Moser, Simple extension of the plane-wave final state in photoemission: Bringing understanding to the photon-energy dependence of two-dimensional materials, Phys. Rev. Res. **5**, 033075 (2023).

[15] G. Stefanucci and R. van Leeuwen, *Nonequilibrium Many-Body Theory of Quantum Systems: A Modern Introduction*, 2nd ed. (Cambridge University Press, Cambridge, UK, 2025).

[16] J. K. Freericks, H. R. Krishnamurthy, and T. Pruschke, Theoretical description of time-resolved photoemission spectroscopy: Application to pump-probe experiments, Phys. Rev. Lett. **102**, 136401 (2009).

[17] E. Perfetto, D. Sangalli, A. Marini, and G. Stefanucci, First-principles approach to excitons in time-resolved and angle-resolved photoemission spectra, Phys. Rev. B **94**, 245303 (2016).

[18] M. Schüler and M. A. Sentef, Theory of subcycle time-resolved photoemission: Application to terahertz photodressing in graphene, J. Electron Spectrosc. Relat. Phenom. **253**, 147121 (2021).

[19] A. Rustagi and A. F. Kemper, Photoemission signature of excitons, Phys. Rev. B **97**, 235310 (2018).

[20] D. Sangalli, Excitons and carriers in transient absorption and time-resolved ARPES spectroscopy: An *ab initio* approach, Phys. Rev. Mater. **5**, 083803 (2021).

[21] P. Törmä, Essay: Where can quantum geometry lead us? Phys. Rev. Lett. **131**, 240001 (2023).

[22] M. Kang, S. Kim, Y. Qian, P. M. Neves, L. Ye, J. Jung, D. Puntel, F. Mazzola, S. Fang, C. Jozwiak, A. Bostwick, E. Rotenberg, J. Fuji, I. Vobornik, J.-H. Park, J. G. Checkelsky, B.-J. Yang, and R. Comin, Measurements of the quantum geometric tensor in solids, Nat. Phys. **21**, 110 (2025).

[23] S. Cho, J.-H. Park, J. Hong, J. Jung, B. S. Kim, G. Han, W. Kyung, Y. Kim, S.-K. Mo, J. D. Denlinger, J. H. Shim, J. H. Han, C. Kim, and S. R. Park, Experimental observation of hidden Berry curvature in inversion-symmetric bulk $2H-WSe_2$, Phys. Rev. Lett. **121**, 186401 (2018).

[24] M. Schüler, U. De Giovannini, H. Hübener, A. Rubio, M. A. Sentef, and P. Werner, Local Berry curvature signatures in dichroic angle-resolved photoelectron spectroscopy from two-dimensional materials, Sci. Adv. **6**, eaay2730 (2020).

[25] M. Ünzelmann, H. Bentmann, T. Figgemeier, P. Eck, J. N. Neu, B. Geldiyev, F. Diekmann, S. Rohlf, J. Buck, M. Hoesch, M. Kalläne, K. Rossnagel, R. Thomale, T. Siegrist, G. Sangiovanni, D. D. Sante, and F. Reinert, Momentum-space signatures of Berry flux monopoles in the Weyl semimetal TaAs, Nat. Commun. **12**, 3650 (2021).

[26] M. Schüler, U. De Giovannini, H. Hübener, A. Rubio, M. A. Sentef, T. P. Devereaux, and P. Werner, How circular dichroism in time- and angle-resolved photoemission can be used to spectroscopically detect transient topological states in graphene, Phys. Rev. X **10**, 041013 (2020).

[27] I. Adawi, Theory of the surface photoelectric effect for one and two photons, Phys. Rev. **134**, A788 (1964).

[28] P. J. Feibelman and D. E. Eastman, Photoemission spectroscopy—Correspondence between quantum theory and experimental phenomenology, Phys. Rev. B **10**, 4932 (1974).

[29] P. Puschnig, S. Berkebile, A. J. Fleming, G. Koller, K. Emtsev, T. Seyller, J. D. Riley, C. Ambrosch-Draxl, F. P. Netzer, and M. G. Ramsey, Reconstruction of molecular orbital densities from photoemission data, Science **326**, 702 (2009).

[30] C. S. Kern, A. Windischbacher, and P. Puschnig, Photoemission orbital tomography for excitons in organic molecules, Phys. Rev. B **108**, 085132 (2023).

[31] F. Boschini, M. Zonno, and A. Damascelli, Time-resolved ARPES studies of quantum materials, Rev. Mod. Phys. **96**, 015003 (2024).

[32] Z. Ye, T. Cao, K. O'Brien, H. Zhu, X. Yin, Y. Wang, S. G. Louie, and X. Zhang, Probing excitonic dark states in single-layer tungsten disulphide, Nature (London) **513**, 214 (2014).

[33] F. Wu, F. Qu, and A. H. MacDonald, Exciton band structure of monolayer MoS_2, Phys. Rev. B **91**, 075310 (2015).

[34] C. Poellmann, P. Steinleitner, U. Leierseder, P. Nagler, G. Plechinger, M. Porer, R. Bratschitsch, C. Schüller, T. Korn, and R. Huber, Resonant internal quantum transitions and femtosecond radiative decay of excitons in monolayer WSe_2, Nat. Mater. **14**, 889 (2015).

[35] M. Theilen, S. Kaidisch, M. Stettner, S. Zajusch, E. Fackelman, A. Adamkiewicz, R. Wallauer, A. Windischbacher, C. S. Kern, M. G. Ramsey, F. C. Bocquet, S. Soubatch, F. S. Tautz, U. Höfer, and P. Puschnig, Observing the spatial and temporal evolution of exciton wave functions in organic semiconductors, Phys. Rev. X **16**, 031054 (2026).

[36] D. Sangalli, E. Perfetto, G. Stefanucci, and A. Marini, An *ab-initio* approach to describe coherent and non-coherent exciton dynamics, Eur. Phys. J. B **91**, 171 (2018).

[37] A. Marini, E. Perfetto, and G. Stefanucci, Coherence and decoherence in the time-resolved ARPES of realistic materials: An *ab-initio* perspective, J. Electron Spectrosc. Relat. Phenom. **257**, 147189 (2022).

[38] M. Dauth, M. Wiessner, V. Feyer, A. Schöll, P. Puschnig, F. Reinert, and S. Kümmel, Angle resolved photoemission from organic semiconductors: Orbital imaging beyond the molecular orbital interpretation, New J. Phys. **16**, 103005 (2014).

[39] A. Damascelli, Probing the electronic structure of complex systems by ARPES, Phys. Scr. **T109**, 61 (2004).

[40] D. G. Truhlar, P. C. Hiberty, S. Shaik, M. S. Gordon, and D. Danovich, Orbitals and the interpretation of photoelectron spectroscopy and (e,2e) ionization experiments, Angew. Chem. **131**, 12460 (2019).

[41] A. I. Krylov, From orbitals to observables and back, J. Chem. Phys. **153**, 080901 (2020).

[42] P. Puschnig and C. Ambrosch-Draxl, Excitons in organic semiconductors, C. R. Phys. **10**, 504 (2009).

[43] P. Puschnig, E.-M. Reinisch, T. Ules, G. Koller, S. Soubatch, M. Ostler, L. Romaner, F. S. Tautz, C. Ambrosch-Draxl, and M. G. Ramsey, Orbital tomography: Deconvoluting

photoemission spectra of organic molecules, Phys. Rev. B **84**, 235427 (2011).

[44] D. Lüftner, T. Ules, E. M. Reinisch, G. Koller, S. Soubatch, F. S. Tautz, M. G. Ramsey, and P. Puschnig, Imaging the wave functions of adsorbed molecules, Proc. Nat. Acad. Sci. USA **111**, 605 (2014).

[45] A. Haags, D. Brandstetter, X. Yang, L. Egger, H. Kirschner, A. Gottwald, M. Richter, G. Koller, F. C. Bocquet, C. Wagner, M. G. Ramsey, S. Soubatch, P. Puschnig, and F. S. Tautz, Tomographic identification of all molecular orbitals in a wide binding-energy range, Phys. Rev. B **111**, 165402 (2025).

[46] P. Puschnig and D. Lüftner, Simulation of angle-resolved photoemission spectra by approximating the final state by a plane wave: From graphene to polycyclic aromatic hydrocarbon molecules, J. Electron Spectrosc. Relat. Phenom. **200**, 193 (2015).

[47] S. Moser, An experimentalist's guide to the matrix element in angle resolved photoemission, J. Electron Spectrosc. Relat. Phenom. **214**, 29 (2017).

[48] D. Lüftner, S. Weiß, X. Yang, P. Hurdax, V. Feyer, A. Gottwald, G. Koller, S. Soubatch, P. Puschnig, M. G. Ramsey, and F. S. Tautz, Understanding the photoemission distribution of strongly interacting two-dimensional overlayers, Phys. Rev. B **96**, 125402 (2017).

[49] I. Sidilkover, Y. Yen, S. W. D'Souza, J. Schusser, A. Pulkkinen, C. R. Rotundu, M. Hashimoto, D. Liu, Z.-X. Shen, J. Minár, M. Schüler, H. Soifer, and J. A. Sobota, Reexamining circular dichroism in photoemission from a topological insulator, Phys. Rev. Res. **7**, 033027 (2025).

[50] J. H. Ryoo and C.-H. Park, Lippmann-Schwinger approach for accurate photoelectron wave functions and angle-resolved photoemission spectra from first principles, Phys. Rev. Lett. **135**, 056403 (2025).

[51] X. Blase, I. Duchemin, D. Jacquemin, and P.-F. Loos, The Bethe–Salpeter equation formalism: From physics to chemistry, J. Phys. Chem. Lett. **11**, 7371 (2020).

[52] J. Deslippe, G. Samsonidze, D. A. Strubbe, M. Jain, M. L. Cohen, and S. G. Louie, BERKELEYGW: A massively parallel computer package for the calculation of the quasiparticle and optical properties of materials and nanostructures, Comput. Phys. Commun. **183**, 1269 (2012).

[53] T. Galvani, F. Paleari, H. P. C. Miranda, A. Molina-Sánchez, L. Wirtz, S. Latil, H. Amara, and F. Ducastelle, Excitons in boron nitride single layer, Phys. Rev. B **94**, 125303 (2016).

[54] A. J. Uría-Álvarez, J. J. Esteve-Paredes, M. A. García-Blázquez, and J. J. Palacios, Efficient computation of optical excitations in two-dimensional materials with the XATU code, Comput. Phys. Commun. **295**, 109001 (2024).

[55] P. Giannozzi, S. Baroni, N. Bonini, M. Calandra, R. Car, C. Cavazzoni, D. Ceresoli, G. L. Chiarotti, M. Cococcioni, I. Dabo, A. Dal Corso, S. de Gironcoli, S. Fabris, G. Fratesi, R. Gebauer, U. Gerstmann, C. Gougoussis, A. Kokalj, M. Lazzeri, L. Martin-Samos, *et al.*, QUANTUM ESPRESSO: A modular and open-source software project for quantum simulations of materials, J. Phys.: Condens. Matter **21**, 395502 (2009).

[56] P. Giannozzi, O. Andreussi, T. Brumme, O. Bunau, M. B. Nardelli, M. Calandra, R. Car, C. Cavazzoni, D. Ceresoli, M. Cococcioni, N. Colonna, I. Carnimeo, A. Dal Corso, S. de Gironcoli, P. Delugas, R. A. DiStasio, Jr., A. Ferretti, A. Floris, G. Fratesi, G. Fugallo, *et al.*, Advanced capabilities for materials modelling with QUANTUM ESPRESSO, J. Phys.: Condens. Matter **29**, 465901 (2017).

[57] P. Giannozzi, O. Baseggio, P. Bonfà, D. Brunato, R. Car, I. Carnimeo, C. Cavazzoni, S. de Gironcoli, P. Delugas, F. F. Ruffino, A. Ferretti, N. Marzari, I. Timrov, A. Urru, and S. Baroni, QUANTUM ESPRESSO toward the exascale, J. Chem. Phys. **152**, 154105 (2020).

[58] J. P. Perdew, K. Burke, and M. Ernzerhof, Generalized gradient approximation made simple, Phys. Rev. Lett. **77**, 3865 (1996).

[59] A. Kirchhoff, T. Deilmann, P. Krüger, and M. Rohlfing, Electronic and optical properties of a hexagonal boron nitride monolayer in its pristine form and with point defects from first principles, Phys. Rev. B **106**, 045118 (2022).

[60] G. H. Wannier, The structure of electronic excitation levels in insulating crystals, Phys. Rev. **52**, 191 (1937).

[61] M. Weinelt, M. Kutschera, T. Fauster, and M. Rohlfing, Dynamics of exciton formation at the Si(100) $c(4 \times 2)$ surface, Phys. Rev. Lett. **92**, 126801 (2004).

[62] O. Karni, E. Barré, V. Pareek, J. D. Georgaras, M. K. L. Man, C. Sahoo, D. R. Bacon, X. Zhu, H. B. Ribeiro, A. L. O'Beirne, J. Hu, A. Al-Mahboob, M. M. M. Abdelrasoul, N. S. Chan, A. Karmakar, A. J. Winchester, B. Kim, K. Watanabe, T. Taniguchi, K. Barmak, *et al.*, Structure of the moiré exciton captured by imaging its electron and hole, Nature (London) **603**, 247 (2022).

[63] I. Gierz, J. Henk, H. Höchst, C. R. Ast, and K. Kern, Illuminating the dark corridor in graphene: Polarization dependence of angle-resolved photoemission spectroscopy on graphene, Phys. Rev. B **83**, 121408(R) (2011).

[64] E. Krasovskii, *Ab initio* theory of photoemission from graphene, Nanomaterials **11**, 1212 (2021).

[65] S. Kosar and K. M. Dani, Time-resolved photoemission electron microscopy of semiconductor interfaces, Prog. Surf. Sci. **99**, 100745 (2024).

[66] D. Schmitt, J. P. Bange, W. Bennecke, A. AlMutairi, G. Meneghini, K. Watanabe, T. Taniguchi, D. Steil, D. R. Luke, R. T. Weitz, S. Steil, G. S. M. Jansen, S. Brem, E. Malic, S. Hofmann, M. Reutzel, and S. Mathias, Formation of moiré interlayer excitons in space and time, Nature (London) **608**, 499 (2022).

[67] S. Brem, J. Zipfel, M. Selig, A. Raja, L. Waldecker, J. D. Ziegler, T. Taniguchi, K. Watanabe, A. Chernikov, and E. Malic, Intrinsic lifetime of higher excitonic states in tungsten diselenide monolayers, Nanoscale **11**, 12381 (2019).

[68] S. Kaidisch, A. Kleiner, S. Refaely-Abramson, P. Puschnig, and C. S. Kern, Calculation files for "Photoemission tomography of excitons: Momentum-space signatures of correlated electron-hole wave functions" [Dataset], Zenodo, 2026, doi: 10.5281/zenodo.23038913.

[69] A. Bosak, J. Serrano, M. Krisch, K. Watanabe, T. Taniguchi, and H. Kanda, Elasticity of hexagonal boron nitride: Inelastic x-ray scattering measurements, Phys. Rev. B **73**, 041402(R) (2006).

[70] T. Sohier, M. Calandra, and F. Mauri, Density functional perturbation theory for gated two-dimensional heterostructures: Theoretical developments and application to flexural phonons in graphene, Phys. Rev. B **96**, 075448 (2017).

[71] F. H. da Jornada, D. Y. Qiu, and S. G. Louie, Nonuniform sampling schemes of the Brillouin zone for many-electron perturbation-theory calculations in reduced dimensionality, Phys. Rev. B **95**, 035109 (2017).